

Flexible Foil Mesh Generation for Spatial Focal-Body Modeling of a Spherical Mirror

Netzer Moriya

Abstract

We present a novel application of the Flexible Foil Mesh Generation (FFMG) method to model the $3D$ Focal Body generated by a spherical mirror collecting light from an infinitely distant source on its optical axis. The study addresses the challenge of accurately representing highly concave structures formed by the focusing effect. Through theoretical analysis and numerical simulations, we demonstrate the effectiveness of the FFMG method in capturing the intricate geometry of the Focal Body, with implications for computational geometry, $3D$ reconstruction, and optical system modeling.

1 Introduction

1.1 Background

Accurate $3D$ shape modeling is needed in fields such as computational geometry, $3D$ reconstruction, and spatial data analysis. These fields often require the ability to represent both convex and concave structures within a point cloud, particularly in applications where the geometric intricacies of an object are critical. One such example is in optical systems, where various components including shaped mirrors, are used to focus light rays onto a confined volume. The resulting shape, referred to here as a Focal Body (FB), may prove highly concave and poses significant challenges in accurate geometric modeling. One option to capture the geometric structure of such highly concentrated intensity regions can be by referring to close proximities of rays as intersecting points that form a spatially confined point cloud [1, 2]. Traditional methods in computational geometry, such as Convex Hulls or Alpha Shapes, are effective in approximating the outer boundary of a point cloud but often prove insufficient when comes to accurately capturing the complex concave features inherent in Focal Bodies. These limitations can lead to inaccuracies in applications involving optical design, where precise modeling of light paths

and focal regions is crucial. The Flexible Foil Mesh Generation (FFMG) method, originally developed to handle highly concave structures within point clouds [3, 5], offers a promising solution to these challenges. By tending to minimize the surface area while ensuring all (or partial) points within the cloud are enclosed, the FFMG method provides a more accurate representation of complex geometries, making it particularly suited for applications involving concave shapes and ensuring closed surfaces. This study aims to explore the application of FFMG in modeling the 3D Focal Body formed by a spherical mirror, demonstrating its effectiveness in capturing the intricate concave structures that traditional methods struggle to represent.

1.2 Objective

The primary objective of this study is to apply the FFMG method for the precise modeling of the three-dimensional Focal Body formed by the focusing of collimated light along the optical axis of a spherical mirror. The principal aim is to assess the capability of FFMG in accurately representing the complex and highly concave geometry characteristic of the Focal Body. In this study, we define the *Focal Body* as the three-dimensional spatial region formed by the intersection envelope of reflected rays from a spherical mirror, given an infinitely distant collimated light source. This definition relies purely on geometrical optics and does not explicitly incorporate intensity variations or wavefront interference effects. The FB is constructed by tracking the spatial density of ray intersections within a predefined volume, resulting in a highly concave surface representation. This approach ensures a computationally efficient and analytically tractable model, particularly for applications in optical design and computational geometry.

Specifically, this paper seeks to:

1. Develop a detailed methodology for applying the FFMG method to the problem of modeling a Focal Body.
2. Validate the method through numerical simulations.
3. Analyze the performance of FFMG in terms of accuracy, computational efficiency, and its ability to handle concave structures.

1.3 Related Work

3D surface reconstruction is a fundamental problem in computational geometry that involves constructing a surface that approximates the shape of an object based on a set

of sample points, typically obtained from real-world data. This process is crucial in various applications, including computer graphics, medical imaging, and reverse engineering. The challenge lies in accurately capturing both the global shape and fine details, particularly in the presence of noise, outliers, and varying point densities.

Historically, several approaches have been developed to tackle 3D surface reconstruction. One of the earliest and most widely used methods is the *Convex Hull* [6], which constructs the smallest convex shape that encloses all points in the dataset. While simple and computationally efficient, the Convex Hull fails to capture concave regions, making it inadequate for more complex shapes.

To address this limitation, more sophisticated techniques have been developed, including *Delaunay Triangulation* [7] and *Voronoi Diagrams* [8], which are often used to generate a mesh that represents the surface. These methods offer a balance between computational efficiency and accuracy, but they can struggle with highly concave shapes or non-uniform point distributions.

Another notable method is *Alpha Shapes* [9], which extends the concept of the Convex Hull by introducing a parameter that controls the level of detail captured in the shape. This allows for the representation of concavities, but the choice of the alpha parameter can be challenging and may require tuning based on the specific dataset. Also, the method may not guarantee a final closed surface.

Optical systems often involve complex geometries, including highly concave surfaces, where traditional modeling techniques may fail to meet capturing the precise shape and focusing properties.

One of the most fundamental optical components is the *spherical mirror*, which focuses parallel light rays originated from an infinitely distant source at along the optical axis, onto a confined spatial volume (i.e., non-single point) in the vicinity of its optical axis. The shape of the focused light region, referred here as the *Focal Body*, is a three-dimensional structure that reflects the concave shape of the mirror's surface. Accurate modeling of such focal bodies for more complex mirror geometries is essential for predicting and optimizing mirror performance, particularly in applications such as telescopes, laser systems, and imaging devices.

Traditional methods for geometric modeling in optical systems, including ray tracing and wavefront analysis, provide insights into light propagation and focusing behavior. However, these methods often require precise surface models to accurately predict how light interacts with the optical elements. When it comes to representing the Focal Body, traditional surface reconstruction techniques, may not fully capture the concave geometry, leading to potential inaccuracies in optical simulations.

A more detailed discussion on essential methods for generating 3D mesh surfaces from point clouds can be found in [3, 4].

2 Theoretical Background

2.1 A Brief Analysis of Light Distribution Reflected by a Spherical Mirror

2.1.1 Problem Setup

Consider a three-dimensional spherical mirror with an infinitely distant light source positioned along the primary optical axis of the mirror. Given the infinite distance of the source, the incoming rays are parallel to each other and to the primary optical axis. It is assumed that when parallel rays strike a spherical mirror, they reflect according to the law of reflection, where the angle of incidence equals the angle of reflection.

Rays that strike the center of the mirror (on the optical axis) will reflect directly back along the same path. However, rays that strike off-center will reflect at an angle. For simplicity, we assume the light is monochromatic and disregard its wave nature.

2.1.2 Ray Behavior Near the Focal Point

The focal point of the mirror is located at half the radius of curvature. This is a consequence of the mirror equation:

$$\frac{1}{f} = \frac{1}{d_o} + \frac{1}{d_i} = \lim_{d_o \rightarrow \infty} \left(\frac{1}{d_o} + \frac{1}{d_i} \right) = \frac{1}{d_i} \therefore f = d_i \quad (1)$$

where d_o is the object distance (considered infinite for parallel rays) and d_i is the image distance.

From the geometry of spherical mirrors, we know that for parallel rays, the image forms at a distance of $\frac{R}{2}$ from the mirror's surface. Therefore, $d_i = \frac{R}{2}$, and consequently,

$$f = \frac{R}{2} \quad (2)$$

Paraxial rays, which are close to the optical axis, converge near the focal point. For these rays, the small-angle approximation $\sin \theta \approx \theta$ (where θ is the angle of incidence or reflection) holds true, resulting in reflection through or very near to the focal point, which lies at a distance f from the mirror's vertex.

In contrast, rays farther from the optical axis intersect the axis at points closer to the mirror due to spherical aberration. Spherical aberration occurs because non-paraxial rays, which make larger angles with the optical axis, do not adhere closely to the small-angle

approximation. The intersection point z on the optical axis for a ray striking the mirror at a distance y from the optical axis can be formulated by:

$$z = \frac{R \left[1 - 2 \left(\frac{y^2}{R^2} \right) \right]}{\sqrt{1 - \frac{y^2}{R^2}}} \quad (3)$$

where R is the radius of curvature, and y is the height of the incident ray above the optical axis. To simplify this expression, we expand the square root term using a Taylor series for small y/R :

$$\sqrt{1 - \frac{y^2}{R^2}} \approx 1 - \frac{y^2}{2R^2} - \frac{y^4}{8R^4} \quad (4)$$

Substituting this into the expression for z and simplifying, we get:

$$x \approx R \left[1 - \frac{y^2}{R^2} + \frac{y^4}{4R^4} \right] \quad (5)$$

By substituting (2), we obtain the higher-order approximation:

$$z \approx f - \frac{y^4}{16f^3} \quad (6)$$

This approximation shows that non-paraxial rays intersect the optical axis closer to the mirror than the paraxial focal point, with the deviation increasing rapidly with y^4 , reflecting the impact of spherical aberration.

While the approximation in Equation (6) accurately describes small-angle deviations within the paraxial region, its validity diminishes for rays striking the mirror at large angles (i.e., marginal rays with high $\sin \theta \approx \theta$, no longer holds, and higher-order terms in the expansion become non-negligible). Additionally, the assumption that all rays follow a perfect geometric path without considering diffraction or wavefront curvature may introduce further discrepancies in real-world optical applications.

To improve precision in modeling large-angle behavior, alternative numerical strategies such as higher-order aberration corrections, or wavefront-based approaches could be employed. These methods would account for higher-order deviations that are otherwise neglected in the current approximation. Future work could explore such refinements, particularly in applications requiring high-precision optical simulations where marginal ray deviations contribute significantly to focal distortions.

To understand the impact of spherical aberration, we may consider the longitudinal spherical aberration, which represents the difference in the focal lengths between paraxial

rays (close to the optical axis) and non-paraxial rays (farther from the axis). In spherical mirrors, rays near the optical axis converge at the focal length f , where R is the radius of curvature. However, non-paraxial rays intersect the optical axis at points closer to the mirror due to spherical aberration.

For a spherical mirror with radius of curvature R , the focal length for paraxial rays is f . Non-paraxial rays, striking the mirror at a height y from the optical axis, experience spherical aberration, shifting the focal point.

The image distance d_i for such rays can be approximated using:

$$d_i = \frac{R \cos 2\theta}{\cos \theta} \quad (7)$$

where $\theta \approx \frac{y}{R}$. Expanding $\cos \theta$ and $\cos 2\theta$ for small y/R :

$$\cos \theta \approx 1 - \frac{y^2}{2R^2}, \quad \cos 2\theta \approx 1 - 2\frac{y^2}{R^2} \quad (8)$$

leads to:

$$d_i \approx R \left(1 - \frac{y^2}{R^2} \right) \quad (9)$$

The longitudinal spherical aberration Δd is:

$$\Delta d = d_i - f = -\frac{y^2}{2R} \quad (10)$$

Thus, the aberration, growing quadratically with y , is (see also below in (13)):

$$\text{Longitudinal aberration} \approx \frac{y^2}{2R} \quad (11)$$

This approximation shows that the aberration grows quadratically with the distance y from the optical axis, indicating that off-axis rays are increasingly affected. The quadratic relationship means that as y increases, the error in the convergence point grows significantly, leading to a spread in the focal point and a corresponding reduction in image sharpness. Minimizing this aberration is crucial in optical design to ensure high-quality image formation.

The paraxial approximation is central to many optical designs because it ensures that rays converge at a common focal point, producing sharp images. However, as rays

deviate from the paraxial region, aberrations like spherical aberration become significant, affecting the quality of the image.

For a more detailed mathematical treatment of these concepts, including the derivation of the expressions for spherical aberration and a deeper understanding of ray tracing through spherical mirrors, refer to [10, 11].

2.1.3 Formation of the Caustic Surface

The envelope of reflected rays forms a caustic surface, which is a region where light intensity is significantly higher due to the concentration of rays. In the context of a spherical mirror, this caustic surface is a result of spherical aberration, where rays that are not paraxial (i.e., rays far from the optical axis) do not converge precisely at the focal point but instead form a curved surface with a cusp.

For a spherical mirror, the caustic surface has a cusp at the focal point and extends from $\frac{3}{4}R$ to R from the mirror's vertex, where R denotes the radius of curvature¹. The shape of this caustic can be understood more deeply by considering the reflection of rays at different distances from the optical axis.

The reflected rays' envelope can be mathematically described using the concept of geometric optics. For a given incident ray at a height y from the optical axis, the reflected ray's angle relative to the optical axis varies with y , leading to a variation in the intersection points along the optical axis. The cusp at the focal point is where the reflected rays are most tightly concentrated, and as we move away from this point, the rays spread out, forming the extended part of the caustic.

The curvature of the caustic surface near the focal point can be analyzed using catastrophe theory [14], which provides a mathematical framework for understanding the cusp and fold structures in such optical systems. Specifically, the caustic is an example of a "cusp catastrophe," where the intensity of light diverges near the cusp.

The distance z along the optical axis where the caustic forms can be expressed as a function of the ray height y [12]:

$$z(y) = f - \frac{y^4}{16f^3} \quad (12)$$

This relationship indicates that as y increases, the intersection point z moves closer to the mirror, contributing to the formation of the caustic surface. The distance from the mirror's vertex to the point on the optical axis where the caustic terminates corresponds

¹ $\frac{3}{4}R$ is approximately the location where the marginal rays (rays hitting the edge of the mirror) cross the optical axis. However, the caustic extends all the way to R

to the mirror's radius of curvature, R .

2.1.4 Spherical Aberration Effects

Rays originating from the outer portions of the mirror, also known as marginal rays, focus closer to the mirror than paraxial rays, leading to the formation of a blur circle instead of a perfect point focus. This phenomenon is known as spherical aberration and occurs because the curvature of a spherical mirror does not perfectly focus all incoming parallel rays to a single point.

1. **Quantitative Analysis of Spherical Aberration:** The difference in focal points between paraxial rays (which are close to the optical axis) and marginal rays (which are farther from the optical axis) is the primary cause of spherical aberration. For a spherical mirror, the focal length for rays at a distance y from the optical axis can be approximated as (see also above in (11)):

$$f(y) = f_0 \left(1 - \frac{y^2}{2R^2} \right) \quad (13)$$

where:

- $f_0 = \frac{R}{2}$ is the focal length for paraxial rays,
- R is the radius of curvature of the mirror,
- y is the distance from the optical axis.

This expression shows that as y increases, the effective focal length $f(y)$ decreases, causing marginal rays to focus closer to the mirror than paraxial rays.

2. **Formation of the Blur Circle:** Due to spherical aberration, rays that are not paraxial do not converge to a single point, leading to the formation of a blur circle on the image plane. The radius of this blur circle r_b can be approximated by assuming that the deviation in focal points, known as longitudinal spherical aberration, grows quadratically with the ray height y on the mirror surface:

$$\Delta d \propto y^2 \quad (14)$$

Given that the maximum ray height is approximately $D/2$, this suggests:

$$\Delta d \propto \left(\frac{D}{2} \right)^2 \propto D^2. \quad (15)$$

The resulting transverse blur (i.e., the blur circle radius) scales with the deviation in the focus position Δd and the ratio D/f_0 , leading to:

$$r_b \sim \Delta d \cdot \frac{D}{f_0} \propto \frac{D^3}{f_0 R}. \quad (16)$$

This captures the essential reason why the blur circle radius grows with the cube of the aperture diameter.

3. **Higher-Order Aberration Terms:** The blur circle’s radius increases with the fourth power of the mirror’s aperture, $r_b \propto D^4$, indicating that spherical aberration is a higher-order aberration². This relationship emphasizes the non-linear nature of the aberration, where small increases in aperture size lead to disproportionately large increases in aberration.
4. **Mitigating Spherical Aberration:** In optical design, spherical aberration can be minimized by using aspherical mirrors or lenses, which have a curvature that varies with the distance from the optical axis. These designs aim to bring all rays to a common focus, thereby reducing the blur circle and improving image quality.

As a result of these aberrations, the anticipated shape of the Focal Body (FB) resembles a **mushroom-like** structure, with a denser, more concentrated region near the optical axis (the *stem*) and a broader, curved caustic envelope extending outward (the *cap*). This morphology is a direct consequence of the gradual deviation of marginal rays, which intersect the optical axis closer to the mirror due to spherical aberration.

For a comprehensive treatment of spherical aberration and other optical aberrations, please refer to [11].

2.2 Flexible Foil Mesh Generation (FFMG)

The Flexible Foil Mesh Generation (FFMG) method [3] constructs high-quality, closed-surface meshes from confined 3D point clouds using a physically-based simulation of flexible foils. It integrates elasticity-driven deformation, pressure-induced contraction, and adaptive snapping to fixed vertices, ensuring geometric fidelity and computational efficiency.

A deformable triangular mesh $\mathcal{M} = (V, F)$ is initialized around the point cloud using a convex hull approximation.

²The D^3 dependency is generally the primary effect seen with spherical aberration, while the D^4 dependency reflects higher-order corrections that become significant as the aperture size increases or as more detailed aberration terms are considered in the optical analysis.

To effectively model the dynamic adaptation of the mesh, we employ a force-equilibrium approach, ensuring that the mesh deforms in response to applied forces without inertia effects. This method guarantees that the mesh conforms to the point cloud while maintaining structural integrity through controlled deformation.

In this formulation, each vertex is treated as a massless node, connected to its neighbors via elastic constraints that regulate local stiffness and prevent excessive distortion. Additionally, an external pressure force drives the contraction of the mesh, mimicking the behavior of a flexible foil minimizing its surface area. To stabilize the evolution, a numerical damping term is introduced, preventing large, unstable steps and ensuring smooth convergence.

The governing equation for vertex motion is given by:

$$0 = f_{\text{elastic},i} + f_{\text{pressure},i} - c \frac{du_i}{dt} \quad (17)$$

where u_i is the spatial position of the i 'th mesh-point vertex, $f_{\text{elastic},i}$ represents elastic restoration forces, $f_{\text{pressure},i}$ accounts for uniform or spatially varying pressure loads, and c is a damping coefficient that stabilizes the simulation.

This ensures a quasi-static evolution rather than a fully dynamic simulation, meaning that the mesh continuously deforms under applied forces without oscillatory motion associated with inertia.

Elasticity is modeled through a vertex-based elastic force formulation, where each vertex is influenced by the relative displacement of its neighbors:

$$f_{\text{elastic},i} = \sum_{j \in N(i)} k_{ij} \left(\frac{\|u_j - u_i\| - L_{ij}}{L_{ij}} \right) \frac{(u_j - u_i)}{\|u_j - u_i\|}, \quad (18)$$

where k_{ij} is the stiffness coefficient, L_{ij} is the rest length of edge (i, j) , and $N(i)$ denotes the neighboring vertices.

Since the model operates in an **overdamped regime**, the acceleration term is neglected, and the motion of vertices is determined purely by the balance of forces as in (17) above.

This formulation ensures that vertex displacements occur in response to external forces without inertial effects, meaning the system continuously evolves towards a lower-energy configuration without oscillatory motion.

The pressure force on each vertex is computed as:

$$f_{\text{pressure},i} = \frac{p \cdot n_f \cdot A_f}{3}, \quad (19)$$

where p is the pressure magnitude exerted on facet f , n_f is the normal of the facet, and A_f is its area. Fixed vertices $V_{\text{fixed}} \subset V$ constrain the deformation, and a snapping mechanism ensures proximity-based vertex alignment.

The mesh evolution follows an explicit Euler integration scheme:

$$v_i^{t+1} = v_i^t + \Delta t \cdot a_i^t, \quad (20)$$

$$x_i^{t+1} = x_i^t + \Delta t \cdot v_i^{t+1}, \quad (21)$$

where Δt is the time step and v_i^t and a_i^t are the velocity and respective acceleration computed from net forces.

To prevent numerical instability, the method enforces a Courant-Friedrichs-Lewy (CFL) condition [16]:

$$\Delta t < \frac{2}{\omega_{\max}}, \quad (22)$$

where ω_{\max} is the highest eigenfrequency of the system.

By iteratively refining the mesh structure through adaptive smoothing and convergence testing, FFMG generates a physically realistic, topologically consistent mesh that conforms to complex point cloud geometries.

Minimal Surface Approximation The physically-based simulation inherently favors minimal-area solutions within the constraints imposed by the fixed vertices. The pressure-driven contraction mimics the behavior of a flexible membrane seeking an energy-minimizing configuration, akin to soap films forming minimal surfaces under boundary constraints. The elastic forces work to maintain structural integrity while minimizing local surface tension, resulting in a final mesh that approximates a constrained minimal surface. While the method does not explicitly solve a minimal surface equation, its dynamic evolution naturally leads to a stable, near-minimal surface configuration, subject to the imposed geometric constraints.

3 Methodology

3.1 Problem Definition

In this study, we seek to accurately determine the 3D Focal Body generated by a spherical mirror focusing light rays from an infinitely distant source along its optical axis. We use

a ray-tracing simulation to follow a set of rays reflected by the mirror and count their mutual intersections as a function of occurrence in $3D$ space. The Focal Body is the region where the reflected rays converge, forming a complex, highly concave structure. Traditional methods struggle to capture the full extent of this concave geometry, which is crucial for precise optical modeling.

Formally, let $P = \{p_1, p_2, \dots, p_n\}$ represent the set of points in $3D$ space that describe the confined volume of the Focal Body. These points are derived from the intersection of reflected light rays with a hypothetical observation plane placed near the focal region. The goal is to construct a surface S^{cc} that:

1. Encloses all points in P , ensuring no points are excluded.
2. Tend to minimizes the surface area while maintaining a concave structure that accurately represents the complex geometry of the Focal Body.
3. Remains closed and non-intersecting to preserve the integrity of the surface, ensuring that the Focal Body is fully encapsulated without self-intersections.

The FFMG method is employed to construct a surface S^{cc} that meets the above criteria by iteratively refining an initial convex hull. The process involves replacing facets on the convex hull with new facets that better approximate the concave geometry of the Focal Body.

Mathematically, the problem can be formulated as finding a surface S^{cc} that approximately minimizes surface area while satisfying the necessary constraints:

$$S^{cc} \approx \arg \min_S \{\text{Area}(S) \mid P \subseteq \text{Int}(S), S \text{ is non-intersecting and closed}\} \quad (23)$$

where $\text{Area}(S)$ represents the surface area of S , and $\text{Int}(S)$ denotes the interior region enclosed by S .

However, the FFMG method does not explicitly solve a minimal surface problem; rather, it approximates a constrained minimal surface through a physically-based simulation. The method relies on pressure-driven contraction and elastic forces to evolve the surface dynamically, tending toward a locally minimal configuration within the constraints imposed by fixed vertices. While this process favors a minimal-area solution, the final surface is shaped by both physical simulation and numerical constraints, leading to an approximate rather than an exact minimization of surface area.

In summary, the problem involves using FFMG to generate a $3D$ surface that closely captures the concave nature of the light convergence in a spherical mirror system. This provides a detailed yet computationally efficient approximation essential for optical design and analysis.

3.2 Ray Tracing Computational Implementation

The Ray Tracing simulation is developed to model and analyze the reflection behavior of light rays interacting with complex, arbitrary-shaped reflecting mirror geometries.

The key features of the simulation include:

- **Mirror Geometry:** The simulation primarily focuses on cylindrical mirrors, including configurations with segmented, arbitrarily-shaped mirrors exhibiting cylindrical symmetry. This approach enables the exploration of a wide range of setups, from single mirrors to complex arrays of multiple cylindrical mirrors (see in fig. 1).
- **Efficiency through Simplification:** To maintain computational efficiency, the simulation employs cylindrical mirrors to approximate non-cylindrical symmetric mirrors. Logical functions are used to determine ray intersections, effectively reducing the simulation's complexity.
- **Optimization and Consistency:** Optimization is applied not at the level of individual mirrors but to the overall system configuration, ensuring consistency with established results for arbitrarily-shaped mirrors and facilitating smooth transitions between different setups.
- **Ray Source and Reflection Dynamics:** The simulation handles multiple light sources, including a primary on-axis source and additional off-axis sources. The ray density is adjusted to account for losses due to mirror segmentation, ensuring accurate reflection modeling.
- **Comprehensive Analysis of Results:** The simulation offers an in-depth analysis of various mirror configurations, including single spherical mirrors, segmented parabolic mirrors, arbitrarily-shaped mirrors, and complex arrays composed of diverse sets of smaller mirrors. This analysis provides valuable insights into how different segmentations and orientations impact the distribution of reflected light.
- **Optimization Techniques:** The simulation includes robust optimization algorithms to adjust the position and orientation of the mirrors, considering various degrees of freedom such as pitch, azimuth, and spatial coordinates, to minimize image distortion and optimize focus.
- **Source and Ray Parameters:** The simulation allows for the configuration of multiple light sources, each with a customizable number of rays. These rays are traced from their sources to the mirrors and ultimately to a planar surface (analogous to a CCD), where the resulting image quality is thoroughly analyzed.

- **Numerical and Analytical Methods:** The simulation employs both numerical and analytical methods for computing ray reflections, ensuring the accuracy and reliability of the results by validating the methods against each other.
- **Output and Analysis:** Detailed outputs, including images and data files, are generated, capturing key metrics such as spot sizes and image quality for different configurations. These outputs are crucial for evaluating the effectiveness of various mirror setups and optimization strategies.
- **planar surface and Focus Optimization:** A specialized module is included for optimizing the planar surface position to minimize spot size, involving calculations of standard deviation (STD) or root mean square (RMS) focus, and adjusting planar surface height to achieve optimal focus.
- **Reflected Rays:** The simulation produces an output matrix that precisely tracks each incoming ray, detailing its interaction with the mirror. This includes the coordinates of the impact point on the reflecting surface and the orientation of the reflected ray in space, all as functions of the specific mirror segment the ray encounters.
- **Ray Intersections:** In the post-simulation analysis, the reflected rays are evaluated against a predefined 3D grid. The simulation records and creates histograms of the number of rays passing through each cell in this grid, providing a detailed spatial distribution of ray intersections.
- **Focal Body Definition:** Utilizing histogrammed layers based on the density of rays (from the highest value down to a predefined minimum, typically greater than 1% of the total incoming rays), a shell-based Focal Body is constructed. Each layer defines a bounded volume encompassing all cells through which rays of that histogram value or higher pass. At this stage, the Focal Body is represented as a point cloud.

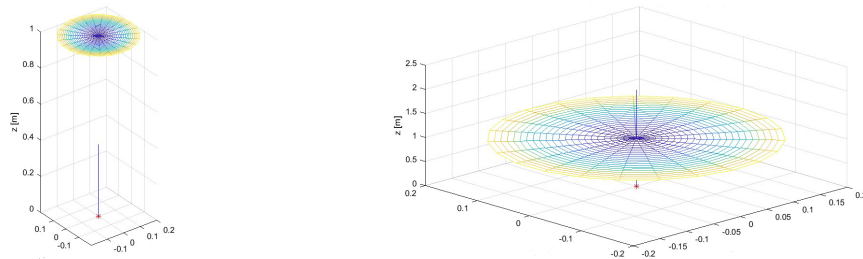


Figure 1: A typical simulation setup for spherical mirror with an equal-axis view (left) and non-equal view (right).

3.3 Application of FFMG to the Focal Body

This section describes the step-by-step application of the Flexible Foil Mesh Generation (FFMG) method to simulate the 3D Focal Body formed by a spherical mirror. The Focal Body is a concave structure resulting from the convergence of light rays reflected by the mirror. The FFMG method generates a mesh that approximates this shape by iteratively refining an initial convex approximation to better conform to the concave geometry of the Focal Body.

3.3.1 Step 1: Initialization with Convex Hull

To ensure consistency in scale, the point cloud is normalized such that each dimension is linearly mapped to the range $[-1, 1]$. This transformation is defined as:

$$\tilde{p}_i = \frac{2(p_i - p_{\min})}{p_{\max} - p_{\min}} - 1, \quad (24)$$

where p_{\min} and p_{\max} denote the minimum and maximum values along each dimension, respectively. As a result, all points satisfy:

$$\tilde{p}_i \in [-1, 1]^d, \quad (25)$$

ensuring a standardized representation for mesh reconstruction.

Following the normalization stage, the convex hull S^{ch} of the point cloud P is computed. This convex hull serves as the initial approximation of the surface, representing the starting boundary of the Focal Body:

$$S^{ch} = \text{Conv}(P) = \bigcap \{H \mid H \text{ is convex, } P \subseteq H\}. \quad (26)$$

While this surface encloses all points in P , it does not capture the concave regions of the Focal Body and requires further refinement.

3.3.2 Step 2: Convex Hull Refinement

After computing the convex hull S^{ch} , the next step involves refining the mesh by introducing denser triangular facets, particularly in regions near the convex hull vertices. The goal of this refinement is to increase the resolution of the initial approximation before applying further deformation.

The refinement process subdivides the triangular facets of S^{ch} by introducing new vertices along edges and within selected facets. This is achieved through a recursive subdivision method that maintains the integrity of the convex hull while ensuring a more uniform and adaptable triangulation.

A key aspect of this refinement process is the adaptive density increase near convex hull vertices. Let v_i be a vertex in S^{ch} , and let $N(i)$ be the set of neighboring vertices. To determine whether refinement is needed, a local density criterion is applied:

$$L_i = \frac{1}{|N(i)|} \sum_{j \in N(i)} \|v_j - v_i\|, \quad (27)$$

where L_i represents the average edge length surrounding v_i . A vertex v_i undergoes further subdivision if:

$$L_i > \gamma L_{\min}, \quad (28)$$

where $\gamma > 1$ is a refinement factor, and L_{\min} is the target edge length in high-resolution regions.

Each refined facet is subdivided by inserting midpoints along its edges, generating new triangular facets. For a given triangle (v_i, v_j, v_k) , the midpoints m_{ij}, m_{jk}, m_{ki} are computed as:

$$m_{ij} = \frac{v_i + v_j}{2}, \quad m_{jk} = \frac{v_j + v_k}{2}, \quad m_{ki} = \frac{v_k + v_i}{2}. \quad (29)$$

These midpoints replace the original triangle with four new sub-triangles, maintaining a non-intersecting and closed structure. The subdivision process continues iteratively until the average edge length reaches the desired refinement level.

The refinement stage ensures that the initial convex hull provides a sufficiently detailed starting point for subsequent deformation, allowing the mesh to better conform to concave regions in later stages.

3.3.3 Step 3: Iterative Surface Refinement

Once the initial set of facets has been constructed, the mesh undergoes an iterative refinement process driven by physically-based deformation. The mesh S_t^{cc} at iteration t evolves according to the force balance equation (17).

The vertices positions u_i are updated using explicit time integration equation (20) and the refinement process continues until a convergence criterion is met:

$$\max_{u_i \in V} \|u_i^{t+1} - u_i^t\| < \epsilon, \quad (30)$$

where ϵ is a predefined threshold ensuring that the surface has reached a stable configuration.

3.3.4 Step 4: Modifications and Optimizations

Several modifications and optimizations are applied to improve the quality and stability of the generated surface:

- *Geometric smoothing*: A Laplacian smoothing operator is applied to prevent excessive local deformations:

$$u'_i = u_i + \lambda \sum_{j \in N(i)} (u_j - u_i), \quad (31)$$

where λ is a smoothing parameter, and $N(i)$ represents the neighboring vertices.

- *Adaptive snapping*: Certain mesh-points vertices are constrained to snap onto predefined fixed positions (the point cloud vertices) to align the mesh with the reference geometry:

$$u'_i = \arg \min_{u_j \in V_{\text{fixed}}} \|u_i - u_j\|. \quad (32)$$

- *Topology preservation*: The refinement process maintains a non-self-intersecting constraint to prevent topological inconsistencies.

3.3.5 Step 5: Final Surface Validation

After the iterative refinement process, the final surface S^{cc} is validated to ensure that it meets the expected geometric and topological criteria. This validation consists of:

- *Enclosure test*: Verifying that all points in P satisfy

$$P \subseteq \text{Int}(S^{cc}). \quad (33)$$

- *Self-intersection check*: Ensuring that the surface remains free of self-intersections.

- *Curvature analysis*: Evaluating whether the surface curvature is consistent with the expected concave structure of the Focal Body.

The application of FFMG to the 3D Focal Body involves an iterative process of surface refinement, which transforms an initial convex hull into a concave representation of the Focal Body. The refinement steps, combined with geometric constraints and stability enhancements, ensure that the generated mesh closely approximates the underlying concave geometry while maintaining computational efficiency.

3.4 Computational Complexity Analysis

The Flexible Foil Mesh Generation (FFMG) method involves a series of computationally intensive steps, each contributing to the overall complexity of the simulation. These steps include mesh initialization, force computation, iterative deformation updates, and convergence testing. Below, we present a high-level analysis of the computational complexity associated with the major components of the simulation.

3.4.1 Mesh Initialization and Subdivision

The initial mesh is generated by computing the Convex Hull of the input point cloud, which requires $O(N \log N)$ operations using the QuickHull algorithm. This provides an initial enclosing surface for the Focal Body. To improve resolution, a subdivision process is applied to the mesh, where each triangular face is iteratively divided, increasing the number of elements by a factor of 4^s , where s is the subdivision level. This results in an exponential increase in the number of faces, leading to an approximate computational complexity of $O(M)$, where M denotes the number of faces after subdivision.

3.4.2 Force Computations and Deformation Updates

Each simulation iteration involves computing two primary forces:

1. **Pressure Forces:** These are computed per face, leading to a complexity of $O(M)$.
2. **Elastic Forces:** Modeled using a force-equilibrium system, each vertex interacts with a fixed number of neighboring vertices, leading to a complexity of $O(N)$.

Additionally, vertex displacement updates occur using explicit time integration, which scales as $O(N)$. Since the number of faces and vertices are related by $M \approx 2N$ for typical triangular meshes, the force computation and deformation update complexity is approximated as $O(N)$ per iteration.

3.4.3 Nearest-Neighbor Searches and Snapping

The snapping mechanism ensures that vertices near fixed points are properly aligned during deformation. This requires repeated nearest-neighbor searches, implemented efficiently using a KD-tree with $O(N \log N)$ complexity for tree construction and $O(\log N)$ per query. Given that nearest-neighbor searches are performed for all N vertices, this results in an overall complexity of $O(N \log N)$ per iteration.

3.4.4 Convergence and Iteration Scaling

The simulation progresses over multiple iterations until convergence criteria are met. In each iteration, the maximum vertex displacement is checked against a predefined tolerance, requiring $O(N)$ operations.

In this study, a fixed time-stepping approach is used to update the mesh deformation process. However, for complex concave structures, adaptive time-stepping could offer an alternative strategy to dynamically adjust step size based on deformation rates, improving stability and efficiency.

A key tradeoff exists between fixed and adaptive time-stepping: while fixed time steps ensure predictable iteration counts and easier convergence analysis, they may require excessively small steps to maintain numerical stability, leading to increased computational costs. Conversely, adaptive time-stepping dynamically adjusts Δt based on local deformation magnitudes, potentially accelerating convergence for smoothly evolving regions while preventing overshooting in high-curvature areas.

The total number of iterations is bounded, typically in the range $50 \leq k \leq 500$. Thus, the total computational cost of the simulation is approximately:

$$O(k(N \log N + N)) = O(kN \log N).$$

3.4.5 Overall Complexity Estimate

Summarizing the dominant computational steps:

Since the number of faces after subdivision grows with $M = O(4^s N)$, choosing a high subdivision level significantly increases the computational cost. However, the iterative updates remain the dominant term, making the simulation complexity approximately $O(kN \log N)$ in practical scenarios.

Computation Step	Complexity
Convex Hull Initialization	$O(N \log N)$
Mesh Subdivision	$O(M)$
Force Computation	$O(N)$
Nearest-Neighbor Snapping	$O(N \log N)$
Iterative Updates	$O(kN \log N)$

Table 1: Computational complexity of major steps in the simulation.

3.4.6 Optimization Considerations

To improve computational efficiency, several optimizations can be applied:

- **Reducing subdivision levels** limits exponential mesh growth.
- **Parallelizing force computations** using vectorized operations can reduce per-iteration costs.
- **Sparse data structures** can be used to minimize unnecessary computations on inactive regions of the mesh.
- **Adaptive time-stepping** can reduce the number of required iterations by dynamically adjusting the deformation step size.

The computational complexity of the FFMG simulation is primarily governed by the number of vertices, faces, and the number of iterations required for convergence. The nearest-neighbor search and force computations dominate each iteration, leading to an overall complexity of $O(kN \log N)$. The framework remains computationally feasible for large-scale point clouds, but careful selection of parameters such as subdivision level and convergence tolerance is necessary to ensure efficiency.

4 Results

4.1 Simulation Setup

The simulation was designed to model the deformation of a flexible foil under the influence of pressure forces and elastic constraints. The following parameters were employed to ensure numerical stability, realistic physical behavior, and computational efficiency.

4.1.1 Mesh Subdivision and Initialization

- **subdivision_level = 3**: This parameter defines the initial refinement level of the mesh, with higher values leading to a finer discretization of the foil. A subdivision level of 3 ensures a balance between computational efficiency and geometric accuracy. Typically, values range from **1** (coarse) to **5** (very fine), where higher levels improve resolution but increase computational cost.

4.1.2 Pressure and External Forces

- **PR_in = 0.5, PR_out = 1.0**: These parameters represent the internal and external pressure applied to the foil, respectively. The net pressure difference, defined as $P = PR_{in} - PR_{out}$, determines whether the structure expands or contracts. In this setup, $P = -0.5$ induces a compressive effect on the foil.
- **pressure_scaling_factor = 10.0**: This factor amplifies the magnitude of pressure forces to ensure they have a significant impact on deformation. Typical values range from **1** to **50**, depending on the scale of the model and the physical properties of the material.
- **Pressure force mode = globalCoM**: Specifies the methodology used to compute pressure force directions. The **global center of mass (globalCoM) method** ensures forces act consistently relative to the centroid of the fixed vertices. Alternative modes, such as *Norm* (face-normal based) or *localCoM* (local neighborhood-based), may be used for different physical behaviors.

4.1.3 Incremental Pressure Application

- **pressure_increment = 0.03**: Defines the incremental increase in applied pressure per iteration. This gradual application prevents numerical instability. Values are typically **0.01–0.05**, depending on the required resolution of deformation tracking.

4.1.4 Snapping and Mesh Constraints

- **snapping_tolerance = 0.02**: Controls the maximum allowable distance for a mesh vertex to be snapped to a fixed vertex. Ensuring snapping within this tolerance prevents artificial stretching or discontinuities. Values range from **0.001** (strict) to **0.05** (loose).

- **max_NNsnapping_iterations = 5**: Specifies the number of iterations allowed for nearest-neighbor snapping relaxation, preventing excessive distortions due to sudden vertex movements.

4.1.5 Deformation Criteria and Convergence

- **deformation_tolerance = 1e-5**: Defines the **convergence criterion** for the simulation. The deformation process halts when the maximum displacement of all vertices falls below this threshold. Values typically range from 10^{-6} (very strict) to 10^{-3} (loose).
- **mTol = 0.016**: This parameter constrains the **maximum allowable displacement** per iteration to prevent excessive motion. It is set to 80% of *snapping_tolerance*, ensuring controlled deformation.

4.1.6 Temporal Resolution and Iterative Processing

- **deformation_max_iterations = 200**: The **maximum number of deformation iterations** before termination. Higher values allow more gradual convergence but increase computational time. This is typically set between **50 and 500**, depending on simulation complexity.
- **dt = 0.03**: The **time step** used for numerical integration. It determines how much the simulation progresses per iteration. A smaller *dt* results in finer temporal resolution but requires more iterations. Typical values are **0.01–0.05**.

4.1.7 Smoothing and Damping Mechanisms

- **smoothingIterations = 1**: Defines the number of **Laplacian smoothing** passes applied to the mesh to prevent noise artifacts. A value of **0** disables smoothing. When used, it typically ranges from **1 to 5**.
- **smoothingTol = 0.02**: Controls the extent of **smoothing influence**, ensuring excessive mesh modification does not occur. It is linked to *snapping_tolerance*.
- **damping_factor = 1.0**: Regulates **force dissipation**, reducing oscillations in vertex movement. A value of **1.0** means no damping, while values below **0.5–0.8** introduce significant damping to stabilize simulations.

4.1.8 Elasticity and Structural Constraints

- **apply_snapping = True**: Enables the snapping mechanism, ensuring vertices within *snapping_tolerance* are relocated to the nearest fixed vertex, preventing unintended distortions.
- **stiffness = 0.01**: Controls the **elastic resistance** of the foil. A value of **0** removes elasticity, while higher values (e.g., **0.05–0.2**) make the foil more resistant to deformation.
- **strain_factor = 10**: Modulates the **stiffness response to stretching**. Increasing this value amplifies stiffness at larger strains. Values typically range from **5 to 15**, depending on material behavior.
- **max_strain = 0.7**: Specifies the **maximum allowable strain** before additional stiffness adjustments occur. Values in the range of **0.5–1.0** provide stability without over-restricting deformation.
- **distance_factor_strength = 1**: Controls the **rate at which fixed vertex influence decays with distance**. Lower values expand the region affected by fixed vertices, while higher values localize their effect.

4.2 Mesh Deformation Results

Figure 2 illustrates the initial, normalized point cloud utilized in this study, representing the spatial distribution of the focal body. The concave structure is evident. The objective of the mesh deformation process is to generate a closed-surface mesh that accurately conforms to the shape defined by the point cloud.

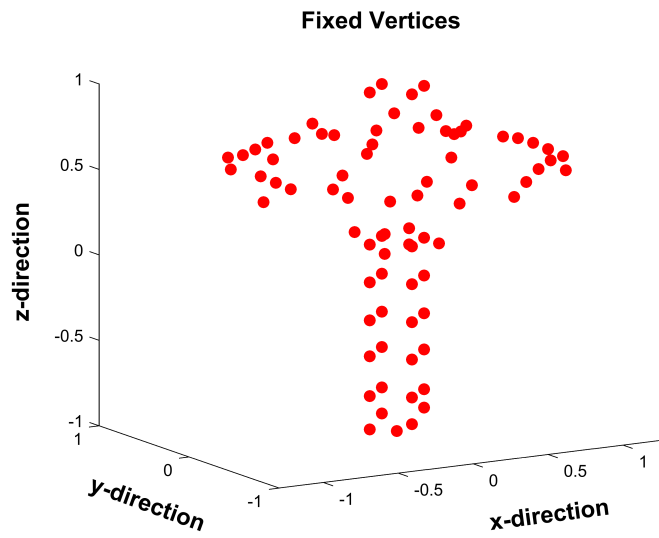


Figure 2: Initial point cloud representing the focal body.

The simulation was initiated using the convex hull as the initial approximation of the mesh 3.

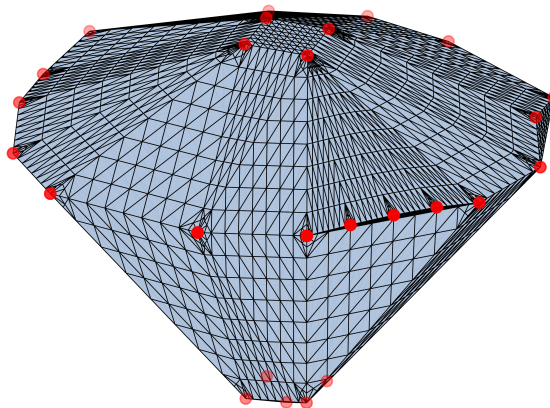


Figure 3: Mesh initialization including Convex Hull vertices and refined mesh in their proximity.

Throughout the iterative process, the mesh undergoes deformation to progressively adhere to the underlying point cloud structure. Figure 4 illustrates the evolution of the mesh at selected iterations 50, 100, 150, and 199.

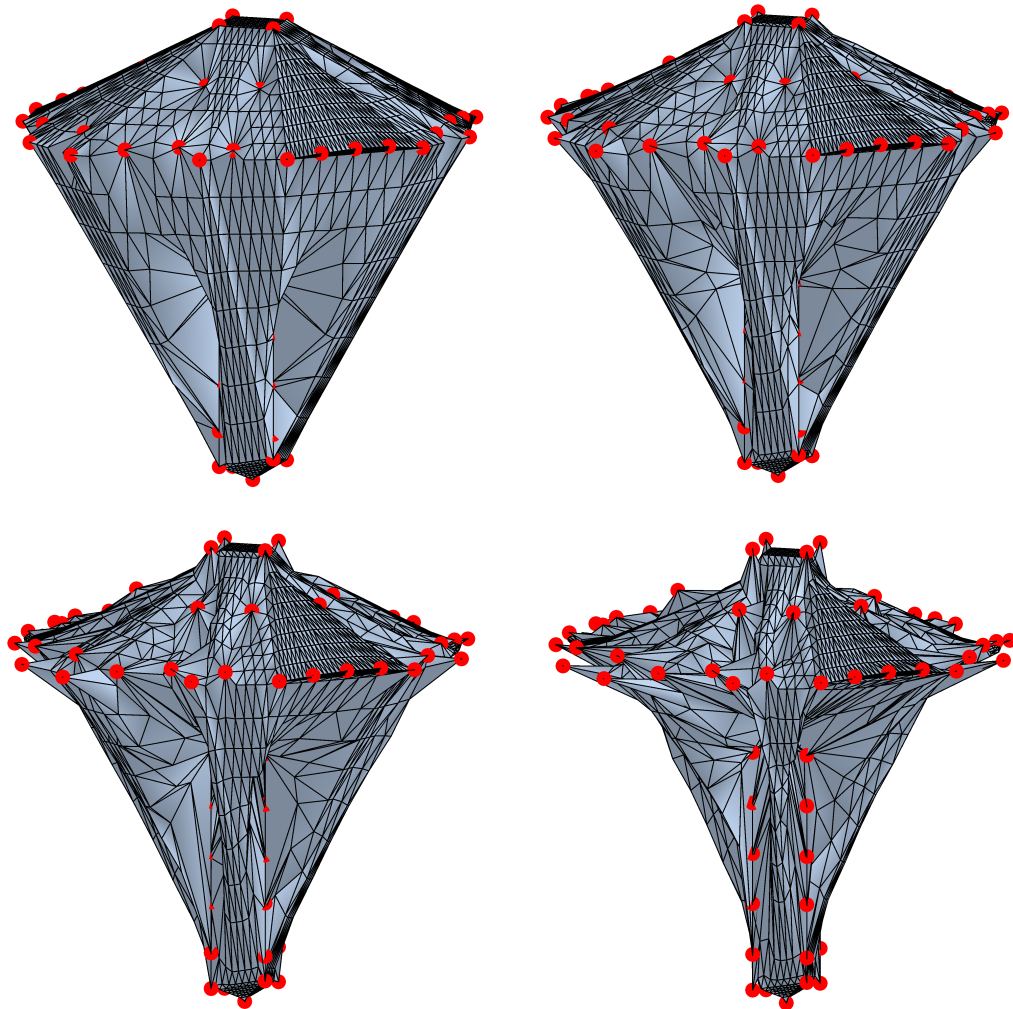


Figure 4: Mesh deformation progression at 50 (upper-left), 100 (upper-right), 150 (lower-left), and 199 (lower-right) iterations.

For additional visualization, refer to the following video demonstration, [click here](#) to watch the simulation video.

The results demonstrate that the evolving mesh conforms to the shape of the point cloud while maintaining closure, ensuring a smooth and topologically consistent repre-

sensation of the focal body.

4.3 Test Point Analysis

To further analyze the mesh deformation process, specific test points were selected across the mesh grid. The forces acting on these points were tracked over the course of the iterations to gain insights into the dynamics of mesh evolution.

Figure 5 presents the spatial components of the pressure force acting on a representative test point as a function of the simulation iterations.

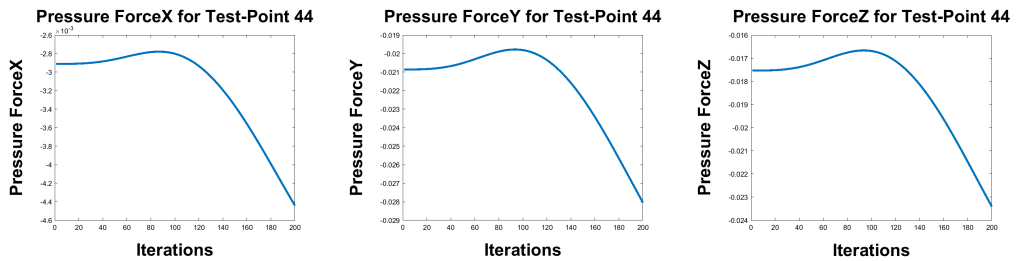


Figure 5: Pressure force components acting on a representative test point during the deformation process.

Similarly, the corresponding elastic force components exerted on the same test point are illustrated in Figure 6.

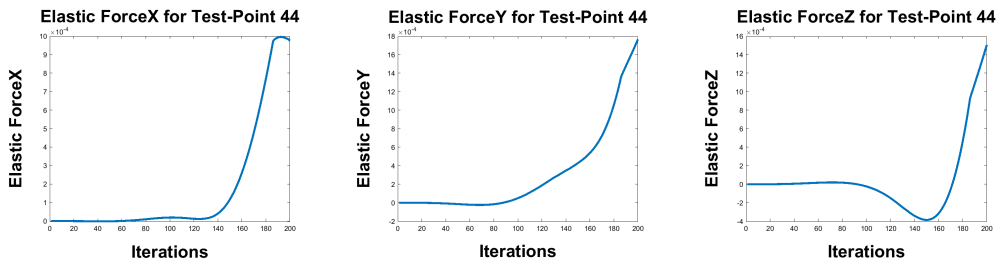


Figure 6: Elastic force components acting on the same test point during the deformation process.

To illustrate the evolution of force magnitudes over time, 3D visualizations of total pressure and elastic forces are provided in Figure 7. These plots depict the force magnitudes along the simulation iterations (Z-axis) with arrows indicating the normalized force direction in 3D space at each time step (X- and Y-axes representing iterations).

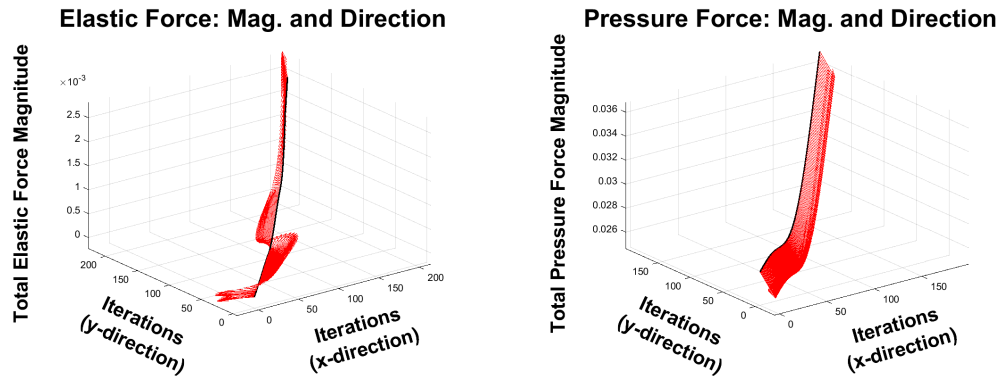


Figure 7: 3D representations of total elastic (left) and pressure (right) force magnitudes and directions over iterations.

Similarly, the total force (elastic + pressure) and the spatial displacement of the test point over iterations are illustrated in Figure 8.

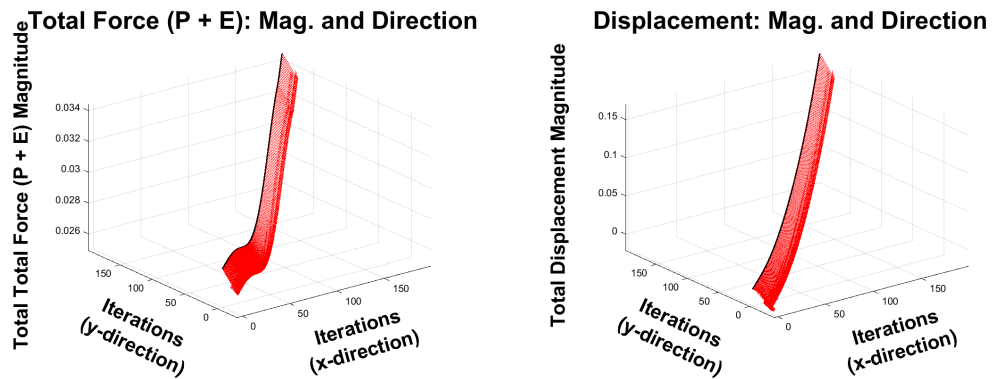


Figure 8: Total force (elastic + pressure) exerted (left) and spatial displacement (right) of the test point over iterations.

Additionally, the evolution of the average nearest-neighbor distance between adjacent mesh points and the change in inner volume of the closed mesh over the simulation iterations are shown in Figure 9.

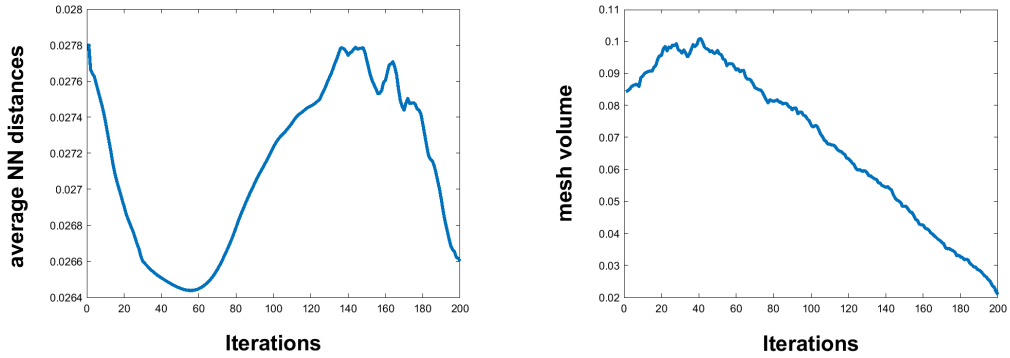


Figure 9: Average nearest-neighbor distance (left) and inner volume of the mesh (right) as functions of simulation iterations.

The results indicate that the deformation process successfully captures the concave characteristics of the focal body while preserving mesh closure and consistency. The iterative force dynamics, as depicted in Figures 5 and 6, show a progressive redistribution of elastic and pressure forces. Although these forces appear to stabilize temporarily, the system does not necessarily settle into a fully steady-state configuration. Instead, the evolution of the mesh continues, particularly in regions where local deformations persist due to ongoing force imbalances.

From a theoretical perspective, the simulation adheres to the principles of force balance between pressure-induced contraction and elasticity-driven restoration. Given that the pressure force dominates initially, the mesh undergoes substantial contraction before reaching a configuration where forces momentarily balance. However, due to the continuous adaptation of the mesh, the system does not reach a final steady-state but remains dynamically evolving. While this process reduces the total surface area, it does not strictly minimize surface area in the mathematical sense of a minimal surface.

An important observation is the relationship between mesh volume reduction and the nearest-neighbor distance evolution, as seen in Figure 9. The contraction theorem discussed earlier (see also in [5]) suggests that if pressure continuously exceeds elastic resistance, the mesh will eventually collapse to a near-zero volume state, with all cloud points lying on the surface. This aligns with the physical interpretation of an over-contracted flexible foil.

Furthermore, the 3D visualizations in Figures 7 and 8 illustrate the directional consistency of force application over iterations. These results confirm that the method preserves force directionality, ensuring a controlled transition of mesh vertices towards their final configuration.

The findings validate the effectiveness of the FFMG approach for capturing concave structures. The behavior observed under different force conditions aligns with theoretical expectations, providing a strong basis for further refinement of the method, particularly in scenarios where the spatial distribution of the point cloud is characterized by enhanced concave nature.

5 Conclusion

This study introduces and applies the Flexible Foil Mesh Generation method to model the highly concave Focal Body formed by the convergence of collimated light reflected from a spherical mirror. By leveraging a physically-driven mesh deformation process, we demonstrate that FFMG effectively reconstructs complex concave geometries that traditional computational geometry techniques struggle to capture.

The theoretical foundation of FFMG rests on a force-equilibrium damping model, where elastic forces preserve structural integrity, pressure-induced contraction drives surface evolution, and damping stabilizes the convergence process.

Through iterative refinement, the simulated mesh dynamically adapts to the underlying structure of the FB, while ensuring enclosure of the spatially dense regions where reflected rays converge.

This physically-motivated framework presents a significant advancement in surface reconstruction techniques, particularly for highly non-convex point clouds arising in optical, acoustical, and structural simulations.

The specific optical example analyzed, ray tracing of a spherical mirror, highlights the limitations of purely geometrical optics. While the present study focuses on ray intersection density as a proxy for light concentration, a truly comprehensive model of the FB would require incorporating wave optics principles such as diffraction and interference. Future refinements could integrate Huygens-Fresnel diffraction models, intensity-weighted ray tracing, or phase-space representations to better approximate the actual optical energy distribution within the FB.

From a computational standpoint, our analysis of fixed vs. adaptive time-stepping demonstrates that the latter could significantly improve efficiency in the deformation process, especially in regions of high curvature variation. However, care must be taken to prevent overshooting and instabilities in regions where force distributions vary sharply.

The findings from this work are not restricted to optical simulations. The principles underlying FFMG offer a generalized methodology applicable to any domain requiring accurate reconstruction of concave surfaces, including medical imaging (e.g., organ boundary reconstruction), astrophysical simulations, fluid interface modeling, and inverse

shape problems in engineering design. The ability to represent highly concave focal structures with minimal user intervention makes FFMG a promising tool for computational geometry and applied physics.

In conclusion, the effectiveness of FFMG in capturing concave spatial structures provides a foundation for future research, particularly in exploring force-driven surface evolution under varying physical constraints. The ability to intentionally manipulate equilibrium conditions in mesh contraction opens new avenues for optimizing geometrical representations of focal surfaces, wavefront interactions, and even dynamically evolving physical systems.

Further development of hybrid geometric-waveform models could bridge the gap between purely geometric simulations and full optical-field representations, enhancing the accuracy and applicability of FFMG in high-precision domains.

Acknowledgments

The author would like to express sincere gratitude to Dr. H. Primack for his significant contributions to the simulation work presented in this study. Dr. Primack's expertise in computational modeling and his assistance in developing the simulation algorithms were crucial to the successful execution of this research.

References

- [1] Niklas Vaara, Pekka Sangi, Miguel Bordallo López, Janne Heikkilä, A Ray Launching Approach for Computing Exact Paths with Point Clouds. *arXiv:2402.13747 [eess.SP]*, 2024. DOI: <https://doi.org/10.48550/arXiv.2402.13747>.
- [2] Luděk Klimeš and Michal Kvasnička. 3-D network ray tracing. *Geophysical Journal International*, 116(3):726–738, March 1994. <https://doi.org/10.1111/j.1365-246X.1994.tb03293.x>.
- [3] Netzer Moriya, Physically-Based Mesh Generation for Confined 3D Point Clouds Using Flexible Foil Models. *arXiv:2502.06541 [math.OC]*, 2025. DOI: <https://doi.org/10.48550/arXiv.2502.06541>.
- [4] Netzer Moriya, The Largest Empty Sphere Problem in 3D Hollowed Point Clouds. *arXiv:2401.07593 [math.OC]*, 2024. DOI: <https://doi.org/10.48550/arXiv.2401.07593>.

- [5] Netzer Moriya, Form Convex Hull to Concavity: Surface Contraction Around a Point Set. *arXiv:2401.14189 [math.OC]*, 2024. DOI: <https://doi.org/10.48550/arXiv.2401.14189>.
- [6] M. Löffler and M. van Kreveld. Largest and Smallest Convex Hulls for Imprecise Points. *Algorithmica*, 56(2):235–269, 2010. <https://doi.org/10.1007/s00453-008-9174-2> DOI: 10.1007/s00453-008-9174-2.
- [7] P. Su and S.-M. Hu. Three-dimensional Delaunay triangulation algorithms. *Advances in Engineering Software*, 27(1-2):55–60, 1996.
- [8] F. Aurenhammer. Voronoi diagrams—a survey of a fundamental geometric data structure. *ACM Computing Surveys*, 23(3):345–405, 1991.
- [9] H. Edelsbrunner and E. P. Mücke. Three-dimensional alpha shapes. *ACM Transactions on Graphics (TOG)*, 13(1):43–72, 1994.
- [10] G. R. Fowles, *Introduction to Modern Optics*, 2nd ed., Dover Publications, 1975.
- [11] M. Born and E. Wolf, *Principles of Optics*, 7th ed., Cambridge University Press, 1999.
- [12] M. V. Berry and C. Upstill, "Catastrophe Optics: Morphologies of Caustics and Their Diffraction Patterns" *Progress in Optics*, vol. 18, pp. 257-346, 1980.
- [13] J. W. Goodman, *Introduction to Fourier Optics*, 3rd ed., McGraw-Hill, 2005.
- [14] V. I. Arnold. *Catastrophe Theory*. Springer, 1992.
- [15] E. Hecht, *Optics*, 4th ed., Addison-Wesley, 2002.
- [16] R. Courant, K. Friedrichs, and H. Lewy, *Über die partiellen Differenzengleichungen der mathematischen Physik*, *Mathematische Annalen*, 1928.